Investigation of the surface orientation influence on 10-nm double gate GaSb nMOSFETs*

Shaoyan Di(邸绍岩)[1], Lei Shen(沈磊)[1], Zhiyuan Lun(伦志远)[1], Pengying Chang(常鹏鹰)[1], Kai Zhao(赵凯)[1,3,†], Tiao Lu(卢朓)[2], Gang Du(杜刚)[1], and Xiaoyan Liu(刘晓彦)[1,‡]

[1] *Institute of Microelectronics, Peking University, Beijing* 100871, *China*
[2] *CAPT, HEDPS, IFSA Collaborative Innovation Center of Ministry of Education, LMAM & School of Mathematical Sciences, Peking University, Beijing* 100871, *China*
[3] *School of Information and Communication, Beijing Information Science and Technology University, Beijing* 100101, *China*

(Received 28 November 2016; revised manuscript received 20 January 2017; published online 20 February 2017)

The performance of double gate GaSb nMOSFETs with surface orientations of (100) and (111) are compared by deterministically solving the time-dependent Boltzmann transport equation (BTE). Results show that the on-state current of the device with (111) surface orientation is almost three times larger than the (100) case due to the higher injection velocity. Moreover, the scattering rate of the (111) device is slightly lower than that of the (100) device.

Keywords: Boltzmann transport equation, GaSb, surface orientation, double gate

PACS: 72.20.Dp, 71.15.–m, 72.20.–i **DOI:** 10.1088/1674-1056/26/4/047201

1. Introduction

Nowadays the performance of the Si devices can hardly be lifted in a big magnitude by continuously scaling down.[1] The III–V material is very promising to substitute Si to achieve a larger current density[2] due to its much higher mobility.[3] However, the benefit of high injection velocity may be compensated by the lower density of state (DoS) of the III–V material.[4] One way to solve the so-called "DoS bottleneck" problem is to transform the surface orientation of the channel material to lower the subband split from the L valley.[5] To achieve this goal, the energy gap between the Γ valley and the L valleys should be small enough to guarantee that the L valleys are to be populated primarily under the effect of quantum confinement. Some works have demonstrated that devices based on GaSb with a transformation of surface orientation give a relatively higher drive current than other material[6,7] because the L-valley subbands that projected to the Γ point occupy a much lighter transport effective mass. In addition, for complementary metal–oxide–semiconductor (CMOS) application, it is essential to evaluate the properties of GaSb nMOSFETs because GaSb pMOSFETs have already shown excellent performance.[8–10] Solving BTE shows intuitive and detailed properties of the electrons in the transport process. In this paper, a deterministic BTE solver[11–13] is used to investigate the effect of surface orientation transformation on the properties of ultra-short GaSb double gate nMOSFETs.

2. Simulation method & device structure

2.1. Simulation method

Our BTE solver involves a self-consistent Poisson–Schrödinger iteration to consider the quantum confinement effect.[11] Assuming that the device is homogenous along the width direction, the BTE is reduced to one-dimensional (1D) in real space and two-dimensional (2D) in $\boldsymbol{k}$ space. It is solved by a positive flux conservative (PFC) method,[11] and the original BTE is split into a transport part

$$\frac{\partial f_i}{\partial t}+v_i\frac{\partial f_i}{\partial x}+F_i\left(\sqrt{2\omega}\cos\theta\frac{\partial f_i}{\partial \omega}-\frac{\sin\theta}{\sqrt{2\omega}}\frac{\partial f_i}{\partial \theta}\right)=0 \quad (1)$$

and a scattering part

$$\frac{\partial f_i}{\partial t}=\left.\frac{\partial f_i}{\partial t}\right|_{\text{Scat}} \quad (2)$$

by time-splitting technique.[14]

In the scattering integral, the intra-valley acoustic phonon scattering, intra-valley optical phonon scattering, inter-valley optical phonon scattering,[15] polar optical phonon scattering,[16] and surface roughness (SR) scattering[17] mechanisms are considered. The transport part is further split into x-advection

$$\frac{\partial f_i}{\partial t}+v_i\frac{\partial f_i}{\partial x}=0 \quad (3)$$

and $\boldsymbol{k}$-advection

$$\frac{\partial f_i}{\partial t}+F_i\left(\sqrt{2\omega}\cos\theta\frac{\partial f_i}{\partial \omega}-\frac{\sin\theta}{\sqrt{2\omega}}\frac{\partial f_i}{\partial \theta}\right)=0 \quad (4)$$

*Project supported by the National Natural Science Foundation of China (Grant Nos. 61674008, 61421005, and 61404005).
†Corresponding author. E-mail: k.zhao.chn@gmail.com
‡Corresponding author. E-mail: xyliu@ime.pku.edu.cn
© 2017 Chinese Physical Society and IOP Publishing Ltd

by dimensional splitting.[14] The polar coordinate is used in the $\boldsymbol{k}$ space. The variables ω and θ present the kinetic energy of the electrons and the angular grid of the $\boldsymbol{k}$ space, respectively, satisfying

$$k_x = \sqrt{2\omega}\cos\theta,$$
$$k_y = \sqrt{2\omega}\sin\theta. \quad (5)$$

The $\boldsymbol{k}$ space is discretized by 150 non-uniform ω grids (uniform in the magnitude of $\boldsymbol{k}$) and 6 uniform θ grids. The maximum kinetic energy is $150k_BT$. Besides, Pauli's exclusion principle is also considered.

2.2. Device structure

10-nm GaSb nMOSFETs with surface orientations of (100) and (111) are simulated by the deterministic BTE solver. The schematic structure of the device is illustrated in Fig. 1. Structure parameters in detail are listed in Table 1. The band structure and scattering parameters of GaSb are extracted in reference[18–20] and listed in Table 2. Figure 2 shows the illustration of the energy valleys in the Brillouin zone in devices with surface orientations of (100) and (111). The transport directions, as the figure shows, are along the $\langle 001\rangle$ and $\langle 1\bar{1}0\rangle$ orientations, respectively. The valleys in the (100) device, as shown in Fig. 2(b), are classified into 2 types (i.e., the Γ valley and 4-equivalent L valley) and we considered the lowest subband of Γ valley and 2 lowest subbands of 4-equivalent L valleys. Meanwhile in Fig. 2(c) for the (111) device, the L valleys projected to the Γ point are classified to the 2nd type of valley because the confinement effective mass is much heavier than other L valleys so that the subbands can be very close to each other. Consequently, we considered 7 subbands for the 2nd type of valley. The rest of the L valleys are further classified into the 3rd and the 4th type because of their different transport effective masses. Two lowest subbands of these valleys are considered. The effective masses of classified valleys along the transport and confinement directions are calculated according to Ref. [16] and extracted in Table 3.

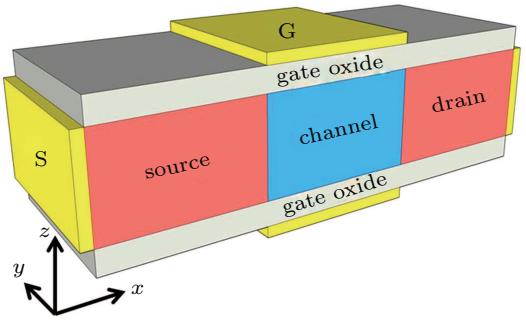


Fig. 1. (color online) The schematic structure of the simulated device. The gate length is 10 nm and the effective oxide thickness (EOT) is 1 nm.

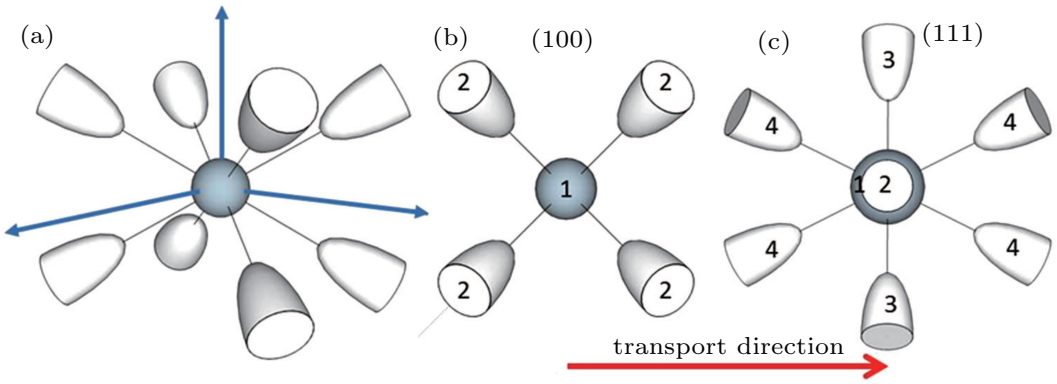


Fig. 2. (color online) (a) The 3D schematic structure of the energy valleys in the Brillouin zone. (b) The projection of energy valleys in devices with surface orientations of (100) and (c) (111). The transport direction is along the (001) and $(1\bar{1}0)$ orientations, respectively. The numbers written on the valleys indicate different types of valleys.

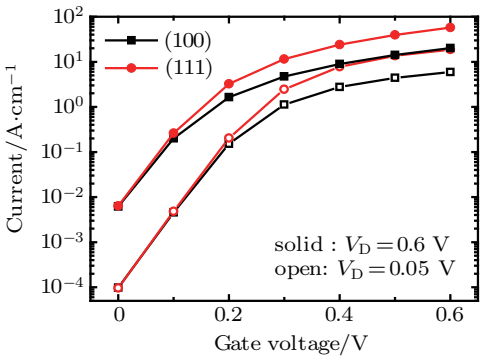


Fig. 3. (color online) The I_D–V_G curves of the simulated devices with (100) and (111) surface orientations.

Table 1. Structure parameters.

Parameters	Values
Channel length/nm	10
S/D length/nm	10
EOT/nm	1
Film thickness/nm	5
Channel doping/cm^{-3}	10^{17}
S/D doping/cm^{-3}	5×10^{19}

Table 2. Band and scattering parameters. m_Γ: the effective mass of Γ valley. m_{Lt}: the transverse effective mass of L valley. m_{Ll}: the longitudinal effective mass of the L valley. $\Delta E_{\Gamma,L}$: the energy gap between the Γ and L valley in bulk material. E_{ac}: the deformation potential of acoustic phonon scattering. ρ: the mass density of material. v_s: the acoustic velocity. Δ_{SR}: the root mean square height of the amplitude of the roughness. L_{SR}: the correlation length. D_o, $\hbar\omega_o$: the deformation potential and the phonon energy of the intra-valley optical phonon scattering. $D_{\Gamma,L}$, $\hbar\omega_{\Gamma,L}$: the deformation potential and the phonon energy of the inter-valley scattering between the Γ valley and L valley. $D_{L,L}$, $\hbar\omega_{L,L}$: the deformation potential and the phonon energy of the inter-valley scattering between different L valleys. ε_0, ε_{indf}: the low frequency and high frequency permittivity.

Parameter	Values	Parameter	Values
m_Γ	$0.042m_0$	D_o/eV·cm^{-1}	2.0×10^8
m_{Lt}	$0.085m_0$	$\hbar\omega_o$/meV	24.0
m_{Ll}	$1.4m_0$	$D_{\Gamma,L}$/eV·cm^{-1}	6.0×10^8
$\Delta E_{\Gamma,L}$/eV	0.085	$\hbar\omega_{\Gamma,L}$/meV	23.8
E_{ac}/eV	6.7	$D_{L,L}$/eV·cm^{-1}	5.7×10^8
ρ/g·cm^{-3}	5.61	$\hbar\omega_{L,L}$/meV	23.8
$v_s/10^5$ cm·s^{-1}	3.24	ε_0	15.69
Δ_{SR}/nm	0.5	ε_{indf}	14.44
L_{SR}/nm	2		

Table 3. Effective masses of classified valleys.

Orientation	Types	Confin. mass (m_0)	Transport mass (m_0)
(100)	1(Γ)	0.042	0.042
	2(L)	0.124	0.156
(111)	1(Γ)	0.042	0.042
	2(L)	1.4	0.085
	3(L)	0.095	0.085
	4(L)	0.095	0.283

3. Results and discussions

The I_D–V_G curves of the simulated devices are shown in Fig. 3. The I_{OFF} in the linear state ($V_D = 0.05$ V) is set to be 10^{-4} A/cm by shifting the work function. The current of (111) device increases faster than that of the (100) device with the gate voltage gradually shifting from 0 V to 0.6 V. The on-currents I_{ON} of the (100) and (111) devices are 20.22 A/cm and 57.73 A/cm, respectively. The electron densities along the channel are illustrated in Fig. 4. The subband profiles are compared in Fig. 5. The lowest subbands of L valleys are lower than the Γ valley which is totally different from the bulk material due to the light confinement effective mass of the Γ valley. For the (111) device, there are much more subbands than in the (100) case due to the much heavier confinement effective masses of the non-degenerate subband originating from the L valley corresponding to the 2nd type in Fig. 2(c). As for the 3-fold degenerate subbands, one corresponds to type 3 and the other two belong to the 4th type due to their different transport effective masses.

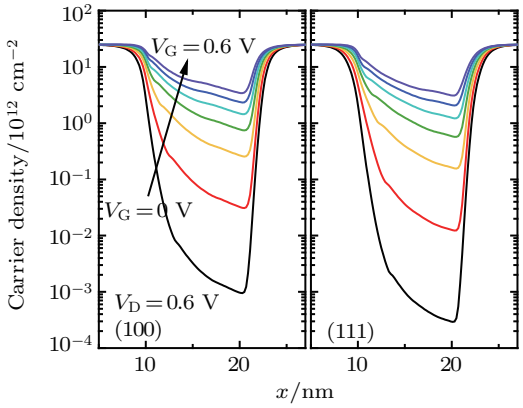


Fig. 4. (color online) The electron density distributions along the transport direction in devices of (100) and (111) surface orientations.

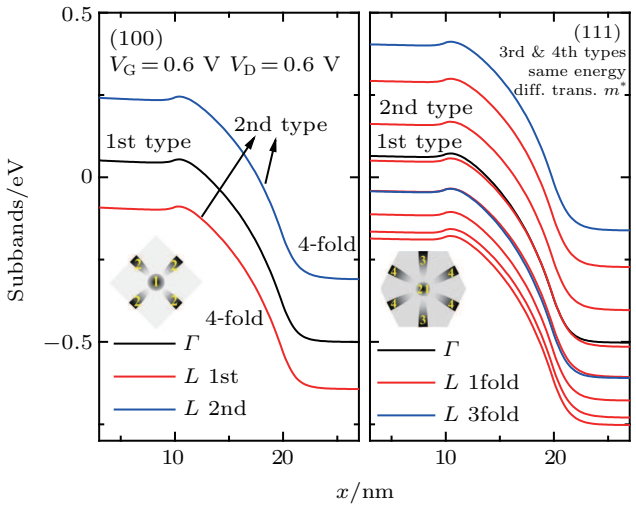


Fig. 5. (color online) The subband profiles of devices under surface orientations of (100) and (111) with $V_G = 0.6$ V and $V_D = 0.6$ V. The insight figures show the Brillouin zone of each case.

3.1. Electron transport

According to the top-of-the-barrier theory,[21] the electron properties at the virtual source are primarily studied. Figure 6(a) shows the carrier density at the virtual source with the increasing gate voltage and the electron's injection velocity at the virtual source is shown in Fig. 6(b). The carrier density of the (111) device increases faster with the gate voltage than the (100) device, especially under higher gate voltage. As for the injection velocity, the (111) device is almost four times larger than that of the (100) device. Moreover, the disparity of two cases becomes larger with the increase of gate voltage. Compared with the injection velocity of the (111) GaSb device simulated in Ref. [7] 1.27×10^7 cm/s, the velocity in our simulation, 2.73×10^7 cm/s, is more than twice as large. The reason can be understood that the smaller transverse electric field brought in by the thicker EOT mitigates the intensity of the surface roughness scattering. In summary, the ratios of the density at the virtual source in the (111) device to that in the (100) device increases from 0.277 to 0.874 with the gate voltage while the ratio of injection velocity stays around 3.5

at every gate voltage. The drive current of the (111) device is consequently larger than that of the (100) device, owing to the fact that the current is determined by the multiplicity of the carrier density and the velocity at the virtual source.

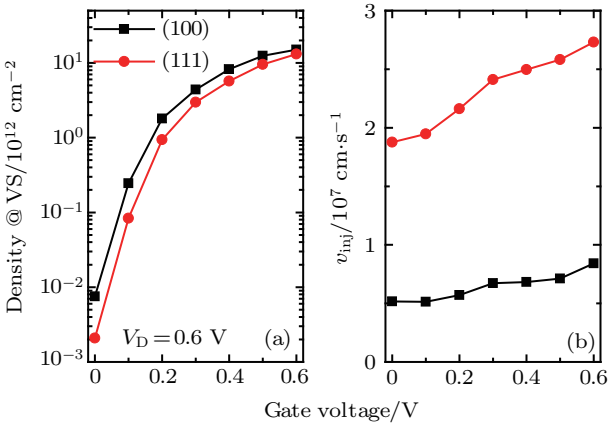


Fig. 6. (color online) The relations of (a) carrier density at the virtual source and (b) the injection velocity at the virtual source with the gate voltage for devices with surface orientations of (100) and (111).

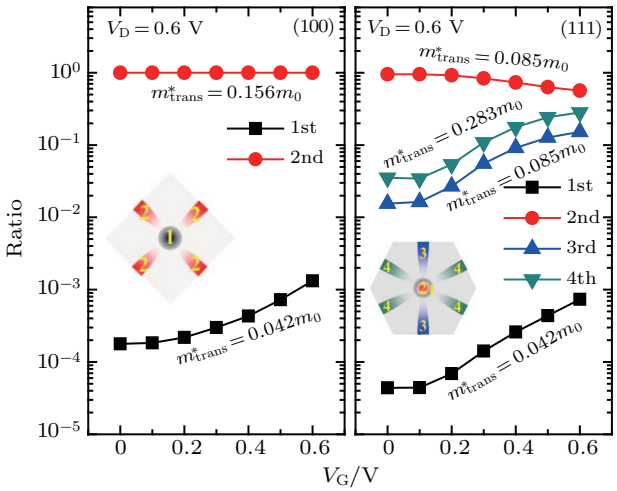


Fig. 7. (color online) The ratio of electrons in different types of subbands at the virtual source. The numbers of subbands in the label and the color of the symbols correspond to the marks in the insight figure. The transport effective masses are marked in the same color with the corresponding symbols.

Figure 7 shows the ratios of electrons in different types of subbands at the virtual source. Electrons mainly populate in L valleys in the device with the surface orientation of (100). The ratio of the electrons residing in the Γ valley increases with the gate voltage but is still much lower than 1% as a result of Γ valley's extremely small density of states. As for the (111) case, the electrons do not populate in the 4 L valleys as is average. The subbands of the 2nd type hold more than 70% of the electrons because the subbands are lower in energy and large in amount. The ratios of the other 3 types of subbands begin to increase when the gate voltage is larger than 0.1 V. It is worth noting that the difference is very large between the transport effective masses of the subbands holding the most electrons in two cases ($0.085m_0$ and $0.156m_0$), which leads to the fact that the injection velocity of the (111) device at the virtual source is much higher than that of the (100) device.

3.2. Scattering

Figure 8 shows the scattering spectra of the two types of devices. The scattering rate in the device with (111) surface orientation is as small as 2×10^{12} s^{-1} with a low kinetic energy, which is far lower than the (100) case reading 3×10^{13} s^{-1} because the density of state of the lowest subband of the (111) device is much smaller than that of the (100) device. Besides, the inter-valley scattering mechanisms do not exist in low energy region due to the non-degeneracy of the lowest subband. The scattering rate of the (111) device increases with the kinetic energy gradually and becomes 6.53×10^{14} s^{-1} which is slightly higher than the (100) case. The ratios of electrons scattered by various scattering mechanisms during the transport process are extracted in Fig. 9. The scattering between L valleys is the most influential mechanism in both cases. When comparing the (111) device with the (100) device, its total scattering ratio is slightly lower but the ballistic ratio ($B = I_{\rm scat}/I_{\rm ball}$) of the (111) device is slightly smaller than the (100) device because more kinetic energy is dissipated by the stronger L–L inter-valley scattering near the drain. The ballistic ratio of the (100) and (111) devices are 91.8% and 87.4%, respectively.

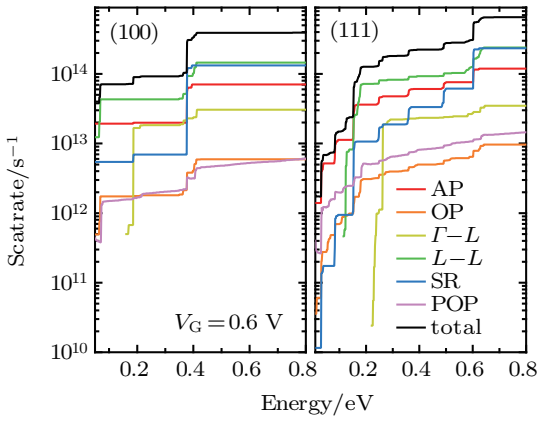


Fig. 8. (color online) Electron scattering rate spectra of devices with surface orientations of (100) and (111). AP: intra-valley acoustic phonon scattering; OP: intra-valley optical phonon scattering; Γ–L: inter-valley optical phonon scattering between Γ and L valleys; L–L: inter-valley optical phonon scattering among L valleys; SR: surface roughness scattering; POP: polar optical phonon scattering; total: total scattering rate.

The distributions of the electron's kinetic energy under on-state are illustrated in Fig. 10. Despite the existence of the scattering, it can be seen from the energy spectrum that the electrons are not relaxed to the equilibrium state after the transport through the channel. This indicates that the electrons' transport in the simulated device is quasi-ballistic and emphasizes the importance of injection velocity to the performance of the device. Moreover, the undissipated energy in the

drain may lead to reliability problems like self-heating problems.

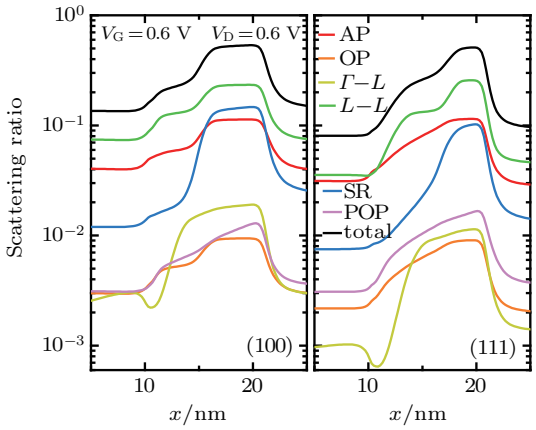


Fig. 9. (color online) The ratios of electrons scattered by different scattering mechanisms along the channel.

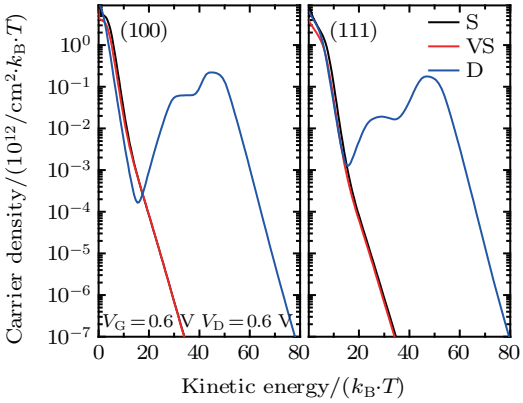


Fig. 10. (color online) The kinetic energy distribution at source, virtual source, and drain of devices with surface orientations of (100) and (111).

4. Conclusion

The performance of 10-nm double gate GaSb nMOSFETs with surface orientations of (100) and (111) are compared by a deterministic BTE solver. Results show that the drive current of the device with a surface orientation of (111) is almost 3 times larger than that of the (100) device as a result of the higher injection velocity at the virtual source. The scattering ratio of devices with (111) surface orientation is less than the (100) devices in the low energy region. The diversity is not obvious when the kinetic energy exceeds 0.2 V.

References

[1] Del Alamo J A 2011 *Nature* **479** 317
[2] Takagi S and Takenaka M 2015 *Solid State Device Research Conference*, September 14–18, 2015, Graz, Austria, p. 20
[3] Kalna K, Yang L and Asenov A 2005 *Solid-State Device Research Conference*, September 16, 2005, Grenoble, France, p. 169
[4] Solomon P M and Laux S E 2001 *IEDM Tech. Dig.*, December 2–5, 2001, Washington DC, USA, p. 95
[5] Rodwell M, Frensley W, Steiger S and Chagarov E 2010 *Proc. Device Research Conference*, June 21–23, 2010, Indiana, USA, p. 149
[6] Kim R, Rakshit T, Kotlyar R and Hasan S 2011 *IEEE Electron Dev. Lett.* **32** 746
[7] Luisier M 2011 *IEEE Electron Dev. Lett.* **32** 1686
[8] Chang P, Liu X, Du G and Zhang X 2014 *IEDM Tech. Dig.*, December 15–17, 2014, San Francisco, USA, p. 7.7.1
[9] Chang P, Zeng L, Liu X and Du G 2015 *Solid State Electronics* **113** 68
[10] Chang P, Liu X, Zeng L and Du G 2015 *Jpn. J. Appl. Phys.* **54** 04DF08
[11] Lu T, Du G, Liu X and Zhang P 2011 *Commun. Comput. Phys.* **10** 305
[12] Di S, Zhao K, Lu T, Du G and Liu X 2016 *J. Comput. Electron.* **15** 770
[13] Di S, Zhao K, Lun Z, Lu T, Du G and Liu X 2016 *IEEE Symp. VLSI-TSA*, April 25–28, 2016, Hsinchu, Taiwan, p. 1
[14] Abdallah N B, Caceres M J, Carrillo J A and Vecil F 2009 *J. Comput. Phys.* **228** 6553
[15] Smirnov S 2003 "Physical Modeling of Electron Transport in Strained Silicon and Silicon-Germanium", Ph. D. dissertation (Wien: Fakultät für Elektrotechnik und Informationstechnik)
[16] Esseni D, Palestri P and Selmi L 2011 *Nanoscale MOS Transistors* (New York: Cambridge University Press) pp. 348–358
[17] Esseni D 2004 *IEEE Trans. Electron Dev.* **51** 394
[18] Damayanthi P, Joshi R P and McAdoo J A 1999 *J. Appl. Phys.* **86** 5060
[19] Ruch J G 1972 *Appl. Phys. Lett.* **20** 246
[20] Dutta P S, Bhat H L and Kumar V 1997 *J. Appl. Phys.* **81** 5821
[21] Lundstrom M S 1997 *IEEE Electron Dev. Lett.* **18** 361